Editors' Suggestion

Nonlocal Ventilating Metasurfaces

Yihuan Zhu,[§] Ruizhi Dong,[§] Dongxing Mao,[*] Xu Wang,[†] and Yong Li[‡]
Institute of Acoustics, School of Physics Science and Engineering, Tongji University, Shanghai 200092, China

(Received 31 October 2022; revised 25 November 2022; accepted 5 December 2022; published 26 January 2023)

Nonlocal metasurfaces, by harnessing the nonlocality, have shown their unparalleled capacities for the efficiency of wave-front manipulation. Here, we demonstrate that nonlocality can be served as a powerful tool to achieve a dramatical enhancement in working bandwidth, showcased by an acoustic open metasurface encoding the exceptional property of allowing airflow while blocking sound transmission. Our design is a binary metaunit composed of two parts, a central orifice and a surrounding helical blade. We show that the transmission spectrum can be tailored by leveraging the hybrid nonlocal effect from the synergy of radiation coupling and direct coupling, the latter provided by a physical connection between the two parts. Verified by simulations and experiments, such a hybrid nonlocal open metasurface consistently blocks more than 90% of incident energy in the range from 600 to 1900 Hz across four adjacent transmission dips. Our finding may pave a way for noise blocking in a flowing-fluid-filled circumstance, more essentially, sets out an efficient approach for broadband wave manipulation in a hybrid nonlocal way.

DOI: 10.1103/PhysRevApplied.19.014067

I. INTRODUCTION

Controlling the flow of waves at will is a long sought-after goal. Metasurfaces stand out as promising tools due to their vanishing size and are now a research area that has attracted increasing attention; they have shown their unparalleled capabilities in tailoring the wave-matter interaction at the deep-subwavelength level. The last decade has witnessed the success of acoustic metasurfaces [1,2] with tremendous unique functionalities, such as anomalous transmission and reflection [3–24], compact absorption [25–30], holographic rendering [31,32], and acoustic topologies [33–35].

Conventionally, acoustic metasurfaces are made up of metaunits, building blocks that are individually designed and then assembled into particular patterns [2]. Although such a design strategy can be considered individual and local, the waves being manipulated are, owing to diffraction, inherently nonlocal. It is therefore found that metasurfaces built in such a way suffer from a limited efficiency on wave-field manipulation [6,20–22].

Among the versatile capabilities of metasurfaces, manipulating waves in a flowing-fluid-filled circumstance is rather challenged. A prime example is a ventilating barrier, which simultaneously blocks sound while allowing free flow of air. Such a device could find widespread use in situations where noise proofing is needed, but airflow needs to be retained, perhaps for cooling or ventilation. Although open acoustic metasurfaces offer a promising solution to the problem [36], the underpinned mechanisms involving local resonance [37] and Fano-like resonance [38,39] inevitably support a narrow working range, owing to the nature of resonance. To overcome this inherent difficulty, a common receipt is to combine multiple detuned resonant elements and "piece together" a wide working bandwidth [40–42].

In this work, we propose a counterintuitive alternative. We show that the enhancement of bandwidth can be realized by leveraging the nonlocality of a metasurface. In the following, we demonstrate that nonlocal effects, induced not only by radiation coupling but also by physical connections among subunits (here called direct coupling), can be utilized as a powerful means in tailoring the transmission spectrum. In more detail, we show that by combining both nonlocal effects in a hybrid fashion, it is possible to extend the bandwidth even further, exemplified by a hybrid-nonlocal design consistently blocking sound over four transmission dips, compared to a prototype built on just radiation coupling, which contains only two transmission dips [43,44]. Our finding suggests an efficient approach for broadband wave engineering empowered by nonlocal metasurfaces.

II. RESULTS AND DISCUSSION

A. Design of a nonlocal ventilating metasurface

The open metasurface investigated in our work is made up of periodically arranged identical metaunits [Fig. 1(a)]. A prototypical metaunit (outer radius $R = 50$ mm, height

[*]dxmao@tongji.edu.cn
[†]xuwang@tongji.edu.cn
[‡]yongli@tongji.edu.cn
[§]Y.Z. and R.D. contributed equally to this work.

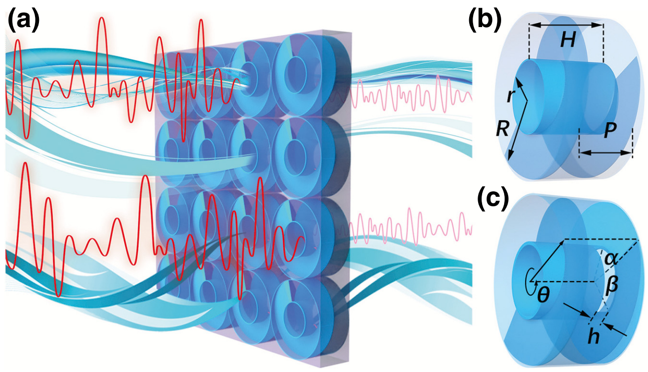

FIG. 1. (a) Diagram of a broadband ventilating barrier made up of periodically arranged nonlocal metaunits. (b) A prototypical nonlocal metaunit composed of a central tube of length H and radius r surrounded by a helix of outer radius R and pitch P. (c) Our modified nonlocal metaunit in which there is an opening between the end of the helical pathway and the tube, which spans both sides of the helical blade. The opening at the rear has a height h, and is divided into two by the blade. Radially, the opening subtends an angle α on one side of the blade and β on the other. [See also the upper panel of Fig. 2(c) for a slightly different view of the placement of the opening.] Opening deviation angle θ is the rotation angle of the opening along the circumference around the cylinder tube axis.

$H = 50$ mm, and pitch $P = 34.542$ mm) is a binary structure comprised of two parts. One part is the central orifice or tube (inner radius $r = 22.5$ mm), which ensures the free flow of air, while the other is a surrounding helical pathway created by the spiral blade [Fig. 1(b)]. The spiral is described by the set of parametric equations, as

$$\begin{aligned} x &= A\cos(\psi), \\ y &= P\psi/2\pi, \quad A \in [r, R], \quad \psi \in [0, 2\pi H/P], \\ z &= A\sin(\psi), \end{aligned} \tag{1}$$

where A and ψ represent the radius and angle of the blade, respectively, and P is a parameter, which describes the pitch of the helix. In this prototype, the two parts are separated by the rigid cylindrical tube.

In principle, such a binary design supports Fano-like interferences, meaning that sound passing through each of the two parts (the central orifice and the surrounding helical path) creates a path difference, so that they destructively interfere and cancel out at the transmitted side [38,39]. In this regard, the presented work blocks sound wave (by reflection) rather than absorbs it, while the intrinsic loss caused by thermal viscosity of the metaunit is rather low. However, such interference naturally indicates that destructive and constructive interferences alternate. In other words, transmission dips indicating effective sound blocking are separated by transmission peaks so that the design, in principle, supports only narrow working bands.

In our previous works [43,44], we have taken a step forward in extending the bandwidth, by utilizing such a prototypical metaunit [Fig. 1(b)]. In these works [43,44], the nonlocality from the radiation coupling between the two parts plays a vital role in realizing broadband sound blocking. In the following, we deliberately introduce another nonlocality and systematically show how dual nonlocality, including radiation coupling as well as direct coupling via physical connections, can be used to tailor the acoustic behavior of a ventilating metasurface.

In this work, numerical simulations are first carried out by using the acoustic pressure module of COMSOL Multiphysics, in the frequency domain to calculate sound transmission through the metasurface. In the simulations, the metaunit is placed in a cylindrical waveguide in which both the waveguide walls and the metaunit itself are considered acoustically rigid. The two ends of the waveguide are set as perfectly matched layers (PMLs), and the background sound field is considered to be an incident plane wave. To calculate the losses caused by viscosity and thermal dissipation, the impedance of a thermoviscous boundary is used in the metaunit.

First, to demonstrate the crucial role that nonlocality plays, we artificially eliminate radiation coupling by extending the central cylindrical tube on both ends of the metaunit, in this case by 40 mm, which will stop the interaction of evanescent waves between the central and surrounding parts. By doing this, the evanescent field attenuates significantly (at least for frequencies whose wavelengths are comparable to the length of the extension) so that the coupling of the two parts, via evanescent fields, can be ignored. For this metaunit with coupling artificially eliminated, the curve of power transmission T (the ratio of transmitted to incident sound energy) shows alternating peaks and dips corresponding to constructive and destructive interferences (dotted lines in the lower panels of Fig. 2). Thus, as expected, because of interference and without any additional nonlocal effect, such a binary design shows only narrow working bands [38,39].

Next, after eliminating the artificially added extension tube, we return to the prototype of the helical metaunit, where radiation coupling naturally occurs at both ends of the metaunit [Fig. 2(a), upper panels]. Generally, in such a nonlocal metasurface, the evanescent fields act so as to channel energy along the surfaces of its two parts [20], and one can observe a significant variation in transmission induced by radiation coupling. Here, similar to the approach adopted in Refs. [45,46], to characterize the performance of the helical metaunit, we numerically calculate its band structure by assuming the metaunit is periodically arranged along the cylinder axis. The lattice constant a is slightly larger than the structure thickness H ($a = 1.1H$ in this case) to avoid two parts (central tube and surrounding helical path) of the metaunit are completely separated so that destructive interference cannot happen.

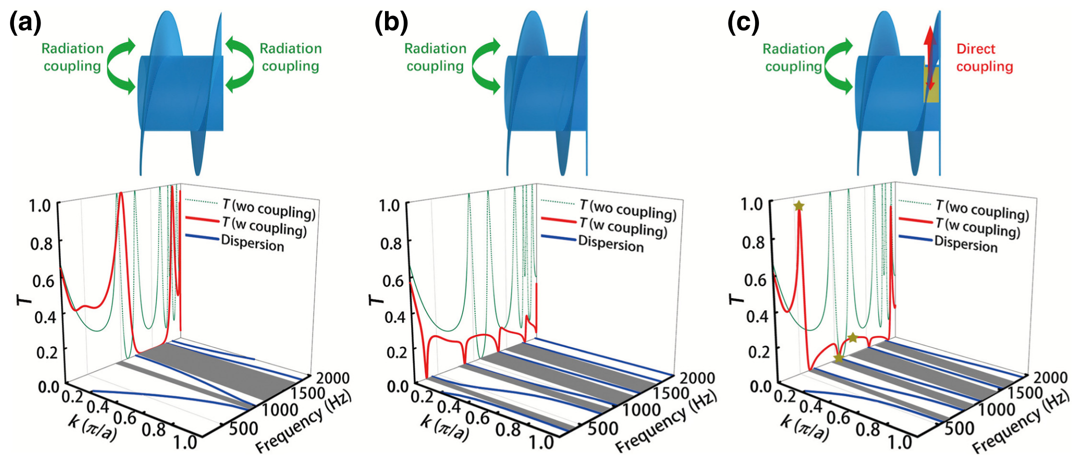

FIG. 2. Band structures (lattice constant $a = 1.1H$) and power transmission curves of three helical designs. (a) The prototypical metaunit featuring radiation coupling on both ends. (b) The modified metaunit in which the helical path at the rear is blocked so that radiation coupling exists only at the front. (c) The proposed metaunit achieved by further adding an opening on the rear center cylindrical tube, which allows both radiation coupling at the front (green arrow) and direct coupling at the rear (red arrow). In all three-dimensional (3D) plots, the dotted green line is the power transmission of a hypothetical metaunit with artificially eliminated radiation coupling by extending the central cylindrical tube, the red line is the power transmission of the illustrated unit, and the blue line is the dispersion curve. The gray areas highlight the corresponding band gaps.

As have been verified by Refs. [45,46], even when only one layer of metaunit is used in practice, the appearance of power transmission attenuation still approximately accords with the gap of the band structure in frequency. As illustrated in the lower panel of Fig. 2(a), a wide band gap (the larger gray region in the bottom plane) appears in the range from 1200 to 1770 Hz, confirmed by the red solid power transmission curve with consistently near-zero sound transmission in this range. This accords with what we have observed in previous works [43,44]. In fact, the sound-blocking band is made up of two consecutive transmission dips at which sound transmission is theoretically zero [43].

One can further manipulate the coupling by covering the rear of the surrounding helical part, leaving only radiation coupling at the front of the metaunit (Fig. 2(b), upper panel). Such single-ended radiation coupling produces two more gaps in the frequency range of interest ($f < 2000$ Hz), giving four in total (gray regions). The corresponding four dips in the power transmission curve are visible as the red line in the lower panel of Fig. 2(b). The increase in the number of transmission dips suggests the possibility of broadening the blocking band by piecing together several dips. Unfortunately, these four band gaps are now separated in frequency, resulting in appreciable sound power transmission ($T > 0.1$) between adjacent dips in the power transmission curve.

The nonlocal metaunit mentioned above uses radiation coupling as a way to channel energy between its different parts. Clearly, nonlocality plays a vital part in engineering the band structure as well as the corresponding power transmission curve. However, it is rather complicated to fine tune the nonlocality induced by radiation coupling. To make use of radiation coupling, a nonlocal metasurface generally requires a complicated reversed-design paradigm—that is, a global optimization method that considers the individual behavior of each part as well as the radiation coupling among them. On the other hand, as an alternative, different parts of a metaunit can be directly coupled using physical connections [47], where the effect of coupling can be tailored by the position as well as the area of connecting channels.

For the helical metaunit, such direct coupling can be achieved by physically linking the central tube and its surrounding helix via an opening in the wall of the tube. Figure 1(c) and the upper panel of Fig. 2(c) illustrate such a design. It is a modification of the single-ended radiation coupling model [Fig. 2(b), upper panel] in which an opening is made close to the rear of the metaunit. The opening can be defined by the following parameters: opening height, h; opening angle, α; opening angle, β, as shown in Fig. 1(c). Such a modified metaunit can, in principle, benefit from radiation coupling at the front as well as direct coupling at the rear. Introducing direct coupling effectively reshapes the band diagram by gathering together the originally widespread four band gaps [gray regions in the lower panel of Fig. 2(c)]. In terms of the power transmission curve, the result is an effective sound attenuation of more than 90% of the incident energy (with a criterion of $T < 0.1$) over the range 600 to 1900 Hz comprising four consecutive transmission dips [red line in the lower panel of Fig. 2(c)].

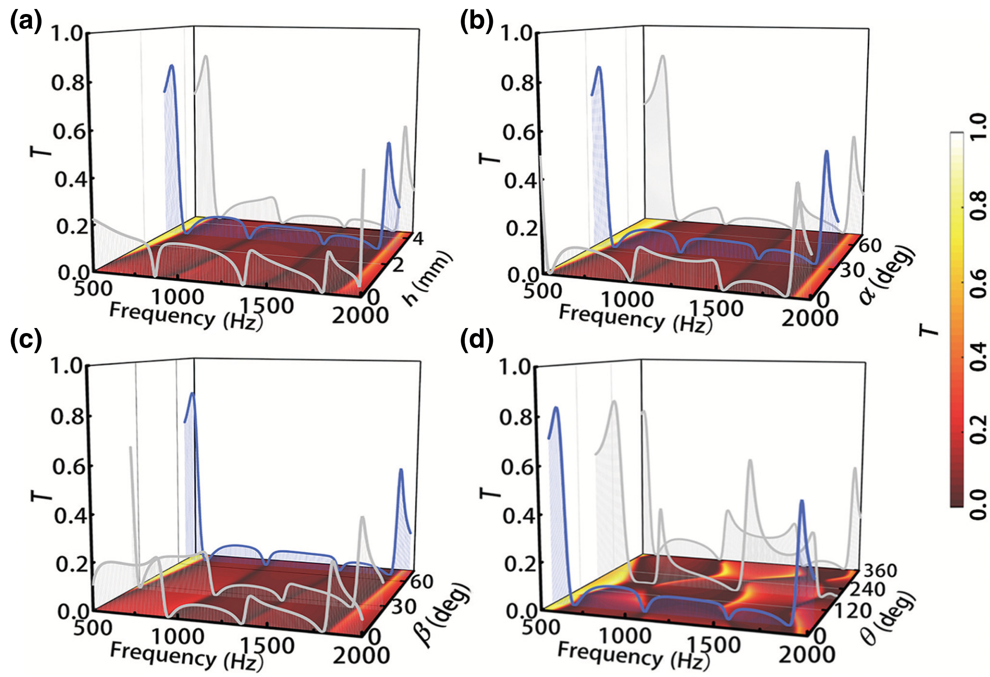

FIG. 3. How direct coupling modifies the transmission spectrum, with each plot showing the effect of varying each of the four structural parameters. (a) Opening height, h. (b) Opening angle width, α. (c) Opening angle width, β. (d) Opening deviation angle, θ. The color maps show the power transmission variation in T as indicated by the scale bar at right, with dark regions indicating effective sound blocking. The isolated profiles show power transmission curves at selected parameters, with blue profiles indicating the optimal design parameters adopted in this work. The designed structural parameters, except for the tuning variable in each diagram, are $h = 3$ mm, $\theta = 0^\circ$, $\alpha = 33.65^\circ$, and $\beta = 66.35^\circ$.

B. Nonlocal effect induced by direct coupling

So far, the effectiveness of direct coupling is demonstrated in an optimal design. In what follows, we look deeper into the effect of direct coupling, with an emphasis on the variation in parameters describing the physical connection, which determines the final behavior of the ventilating metasurface.

The designed ventilating metasurface has radiation coupling at the front and direct coupling at the rear, producing a hybrid nonlocal effect. Crucially, notice that the opening spans across the spiral blade [Fig. 2(c), upper panel], so that the opening permits the central part to directly connect with the helical channel at two different positions, creating two separate sound paths. The two paths provide extra flexibility in tailoring the acoustic behavior of the nonlocal metasurface. Here, to illustrate the ability to customize the transmission spectrum by direct coupling, we systematically investigate the structural parameters of the opening.

First, the area of the opening determines the strength of the direct coupling. This can be most readily tuned by varying the opening height h, while keeping the opening position fixed. As indicated by the color map at the bottom plane of Fig. 3(a), in the parameter space of opening height h and frequency f, dark regions represent effective sound blocking, and the four black lines correspond to the four transmission dips observed in Fig. 2(c) at which sound transmission is theoretically zero. A smaller opening area (smaller h) shows a broader dark region on the frequency axis, together with four transmission dips being more separated, however. Small h, therefore, results in higher levels of sound transmission between the dips, as shown by the gray profile at the front of Fig. 3(a) (compare it with the gray profile at the back). The optimal design with $h = 3$ mm [blue profile in Fig. 3(a)] provides the best balance between the bandwidth and the effectiveness of blocking (again, with a criterion of $T < 0.1$).

The opening permits direct coupling to the surrounding channel at two different positions where the opening intersects the helical blade. In other words, the blade divides the opening into two gaps. There is one gap counterclockwise to the end of the helix (looking from the front), defined by the angle width α, and another gap clockwise to the end of the helix defined by the angle width β [Fig. 1(c)]. The contrast of coupling strengths provided by these two gaps is therefore of interest and is investigated by varying the angles α and β corresponding to the anticlockwise and clockwise parts, respectively, of the opening defined by the helical blade. The optimal result is found for the condition $\alpha = 33.65^\circ$ and $\beta = 66.35^\circ$ [blue profiles in Figs. 3(b) and 3(c)].

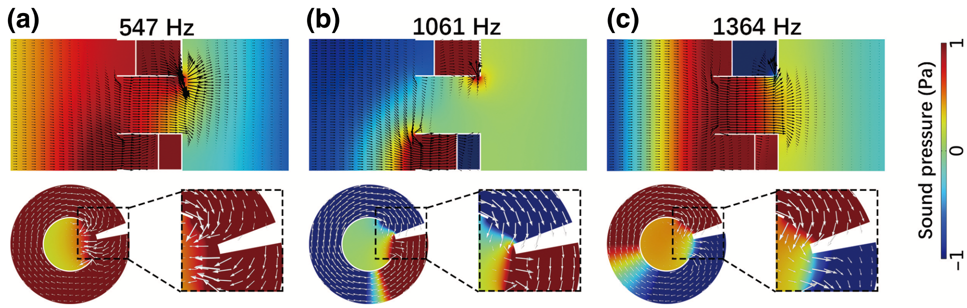

FIG. 4. Simulated sound-field distributions at 547, 1061, and 1364 Hz [the three frequencies marked in lower panel of Fig. 2(c)]. The upper panels are the axial-plane view with the colors indicating the sound pressure and the arrows indicating the energy flows. The lower panels are the radial-plane views of the layer where the opening is located, with the arrows representing intensity and the colors showing acoustic pressure (scale at right).

As aforementioned, the coupling strength is determined by the total opening area, while the coupling strength contrast is governed by the relative areas of the two gaps of the opening. On the other hand, the position, where direct coupling is induced (i.e. the position of the opening), is also crucial for the interplay of central and surrounding parts of the metaunit. Consequently, the opening having a fixed area is then rotated, measured in terms of the angle θ from which the opening deviates from its origin, where $\theta = 360^\circ$ represents a full-round rotation of the opening in the radial plan. The results of varying the deviation angle of the opening demonstrate the power of direct coupling in modulating the transmission spectrum [Fig. 3(d)]. The changes in the color of the heat map indicate that the behavior of the metasurface changes significantly as θ changes. Broadband sound blocking occurs only when the central orifice dually direct coupled to the surrounding helical part, manifested by the opening rotating to those angles (small θ) at which it is intersected by the spiral blade [an optimal case shown by the blue profile at $\theta = 0^\circ$ in Fig. 3(d)].

C. Hybrid nonlocality through radiation coupling and direct coupling

Numerical simulations also provide an intuitive picture of how the system behavior is reshaped by the nonlocality induced by radiation coupling as well as by direct coupling. Figure 4 shows the simulated sound fields at three representative frequencies marked on the power transmission curve of Fig. 2(c), where the first frequency (547 Hz) falls out of while the other two (1061 and 1364 Hz) lying in the sound-proofing band (600–1900 Hz). First, the effect of radiation coupling can be observed by the axial-plane view shown in the upper panels of Fig. 4, where the colors represent sound pressure and the arrows indicate energy flows. Nonlocality by radiation coupling here can be manifested by the strongly distorted arrow surface around the front of the metaunit [Figs. 4(b) and 4(c), upper panels]. Here, higher-order modes carrying evanescent waves serve as a tunnel effectively channeling energy between the central and helical parts. This is a similar behavior to that observed in nonlocal metagratings [20]. Within the working range, a dramatic reduction of pressure amplitude through the metaunit, together with diminishing arrows, gives rise to a silenced zone behind [see colors in green on the transmitted side in the upper panels of Figs. 4(b) and 4(c)].

On the other hand, the nonlocal effect from the direct coupling can be observed by the radial-plan view where the opening is located (Fig. 4, lower panels). Here the arrows represent the sound intensity, and the colors show acoustic pressure distribution. These radial-plan views clearly illustrate how the spiral blade divides the opening into two gaps. The nonlocal behavior induced by direct coupling can be seen as a rapid change in color between the central orifice and the surrounding pathway, as well as by those arrows confirming significant energy exchange through the opening. These arrows illustrate, in detail, how the acoustic flux outflows from the upper gap, pass through the central orifice, and finally inflows into the lower gap [lower panels of Figs. 4(b) and 4(c)].

D. Experimental verification

Experiments are performed to validate the capability of the proposed ventilating metasurface empowered by the hybrid nonlocal effect. A sample of the metaunit is made from photosensitive resin using 3D printing [inset of Fig. 5(a)]. The acoustic characteristics of the metaunit are evaluated by fixing it firmly inside a standard impedance tube (Sinus type-1401), and its sound transmission calculated using the transfer-matrix method (see details in the standard ASTM E2611-09 [48]). The experimental setup is consistent with that adopted for the numerical modeling. Figure 5(b) shows the power transmission of the metaunit, and the results are in excellent agreement with the numerical computations, verifying the effectiveness of our design. Such a ventilation barrier consistently blocks more

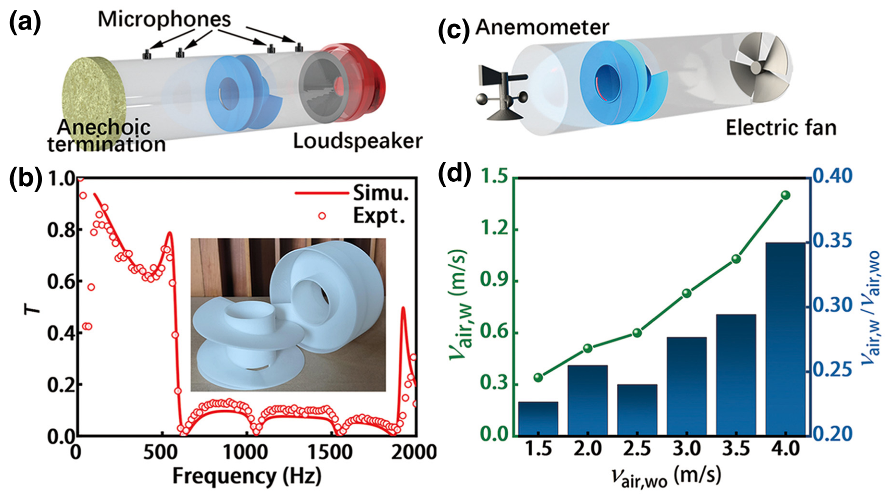

FIG. 5. (a) Experimental setup for evaluating acoustic performance in which a specimen is clamped into an impedance tube. (b) Simulated (solid line) and measured (circles) transmission of the hybrid nonlocal metaunit. The inset is a photo of the 3D-printed specimen. (c) Arrangement for measuring the ventilation characteristics. (d) Measured wind velocities with the unit in place (green line, left axis) and ratios of wind speeds with and without the unit in place (blue bars, right axis).

than 90% of incident sound energy (that is, $T < 0.1$) in the range of 600–1900 Hz (experimental data). Compared to its prototype by leveraging radiation coupling only ($T < 0.1$, 1200–1770 Hz, Fig. 2(a), such a significantly increased bandwidth is due entirely to hybrid nonlocal effects from the synergy of radiation and direct couplings.

Next, the ventilation characteristics of the metaunit are experimentally evaluated [Fig. 5(c)]. An electric fan is placed at the inlet of the waveguide, and the wind speed at the outlet is measured twice, with and without the presence of the metaunit. Figure 5(d) shows the measured ventilation performance, characterized by the ratio of the wind speeds with and without the sample in place. There appears to be a linear dependence on outlet speed, and the velocity ratio is around 27%, demonstrating that airflow is reduced to about a third.

III. CONCLUSIONS

To conclude, we conceptually propose and experimentally validate a broadband ventilating barrier empowered by nonlocal metasurfaces. In particular, we demonstrate the power of nonlocality in engineering the transmission spectrum of the metasurface, endowing a ventilating barrier simultaneously allows the passage of air while consistently blocking sound in a broad frequency range.

In contrast to conventional nonlocal metasurfaces work by means of only radiation coupling or direct coupling, here we show that the hybrid nonlocal effect via the synergy of radiation and direct couplings can be served as a powerful tool for customizing the bandwidth. In this way, we realize a ventilating metasurface enabling an effective blocking of more than 90% of incident energy in the range from 600 to 1900 Hz over four transmission dips, with a structural thickness of only 50 mm (approximately 1/10 of the wavelength of the lower cutoff frequency), while retaining a ventilation fraction of 27%. Beyond those potential applications of ventilating metasurfaces, our finding, more essentially, paves a way for broadband spectrum engineering in an open and nonlocal manner.

ACKNOWLEDGMENTS

This work is supported by the National Science Foundation of China (Grants No. 12074288 and No. 12074286), the Shanghai Science and Technology Committee (Grants No. 21JC1405600, No. 22JC1404100, No. 20ZR1460900, and No. 20ZR1461700), and the Fundamental Research Funds for the Central Universities.

[1] B. Assouar, B. Liang, Y. Wu, Y. Li, J. C. Cheng, and Y. Jing, Acoustic metasurfaces, Nat. Rev. Mater. **3**, 460 (2018).
[2] G. Ma and P. Sheng, Acoustic metamaterials: From local resonances to broad horizons, Sci. Adv. **2**, e1501595 (2016).
[3] Y. Li, B. Liang, Z. Gu, X. Zou, and J. C. Cheng, Reflected wavefront manipulation based on ultrathin planar acoustic metasurfaces, Sci. Rep. **3**, 2546 (2013).
[4] J. Zhao, B. Li, Z. Chen, and C. W. Qiu, Manipulating acoustic wavefront by inhomogeneous impedance and steerable extraordinary reflection, Sci. Rep. **3**, 2537 (2013).
[5] Y. Li, X. Jiang, R. Li, B. Liang, X. Zou, L. Yin, and J. C. Cheng, Experimental Realization of Full Control of Reflected Waves with Subwavelength Acoustic Metasurfaces, Phys. Rev. Appl. **2**, 064002 (2014).
[6] X. Wang, X. Fang, D. Mao, Y. Jing, and Y. Li, Extremely Asymmetrical Acoustic Metasurface Mirror at the Exceptional Point, Phys. Rev. Lett. **123**, 214302 (2019).

[7] S. Fan, S. Zhao, A. Chen, Y. Wang, B. Assouar, and Y. Wang, Tunable Broadband Reflective Acoustic Metasurface, Phys. Rev. Appl. **11**, 044038 (2019).

[8] C. Shen, Y. Xie, J. Li, S. A. Cummer, and Y. Jing, Asymmetric acoustic transmission through near-zero-index and gradient-index metasurfaces, Appl. Phys. Lett. **108**, 223502 (2016).

[9] Y. Li, C. Shen, Y. Xie, J. Li, W. Wang, S. A. Cummer, and Y. Jing, Tunable Asymmetric Transmission via Lossy Acoustic Metasurfaces, Phys. Rev. Lett. **119**, 035501 (2017).

[10] S. Qi, Y. Li, and B. Assouar, Acoustic Focusing and Energy Confinement Based on Multilateral Metasurfaces, Phys. Rev. Appl. **7**, 054006 (2017).

[11] X. Zhu, K. Li, P. Zhang, J. Zhu, J. Zhang, C. Tian, and S. Liu, Implementation of dispersion-free slow acoustic wave propagation and phase engineering with helical-structured metamaterials, Nat. Commun. **7**, 11731 (2016).

[12] Y. Li, X. Jiang, B. Liang, J. C. Cheng, and L. Zhang, Metascreen-Based Acoustic Passive Phased Array, Phys. Rev. Appl. **4**, 024003 (2015).

[13] Y. Li and M. B. Assouar, Three-dimensional collimated self-accelerating beam through acoustic metascreen, Sci. Rep. **5**, 17612 (2015).

[14] Y. Xie, W. Wang, H. Chen, A. Konneker, B. I. Popa, and S. A. Cummer, Wavefront modulation and subwavelength diffractive acoustics with an acoustic metasurface, Nat. Commun. **5**, 5553 (2014).

[15] J. Li, L. Fok, X. Yin, G. Bartal, and X. Zhang, Experimental demonstration of an acoustic magnifying hyperlens, Nat. Mater. **8**, 931 (2009).

[16] J. Zhu, J. Christensen, J. Jung, L. Martin-Moreno, X. Yin, L. Fok, X. Zhang, and F. J. Garcia-Vidal, A holey-structured metamaterial for acoustic deep-subwavelength imaging, Nat. Phys. **7**, 52 (2010).

[17] F. Monticone, C. A. Valagiannopoulos, and A. Alù, Parity-Time Symmetric Nonlocal Metasurfaces: All-Angle Negative Refraction and Volumetric Imaging, Phys. Rev. X **6**, 041018 (2016).

[18] Y. Li, G. Yu, B. Liang, X. Zou, G. Li, S. Cheng, and J. C. Cheng, Three-dimensional ultrathin planar lenses by acoustic metamaterials, Sci. Rep. **4**, 6830 (2014).

[19] Y. Wang, Y. Cheng, and X. Liu, Ultrathin acoustic cloaking by a conformal hybrid metasurface, Sci. Rep. **9**, 12700 (2019).

[20] Z. Hou, X. Fang, Y. Li, and B. Assouar, Highly Efficient Acoustic Metagrating with Strongly Coupled Surface Grooves, Phys. Rev. Appl. **12**, 034021 (2019).

[21] H. Ni, X. Fang, Z. Hou, Y. Li, and B. Assouar, High-efficiency anomalous splitter by acoustic meta-grating, Phys. Rev. B **100**, 104104 (2019).

[22] H. Ding, X. Fang, B. Jia, N. Wang, Q. Cheng, and Y. Li, Deep Learning Enables Accurate Sound Redistribution via Nonlocal Metasurfaces, Phys. Rev. Appl. **16**, 064035 (2021).

[23] C. Hu, B. Liang, J. Yang, and J. Cheng, Experimental demonstration of a three-dimensional omnidirectional and broadband acoustic concentrator using an anisotropic metamaterial, Sci. China Phys. Mech. Astron. **64**, 244304 (2021).

[24] A. Chen, Q. Tang, H. Wang, S. Zhao, and Y. Wang, Multifunction switching by a flat structurally tunable acoustic metasurface for transmitted waves, Sci. China Phys. Mech. Astron. **63**, 244611 (2020).

[25] Y. Li and B. M. Assouar, Acoustic metasurface-based perfect absorber with deep subwavelength thickness, Appl. Phys. Lett. **108**, 063502 (2016).

[26] S. Huang, Z. Zhou, D. Li, T. Liu, X. Wang, J. Zhu, and Y. Li, Compact broadband acoustic sink with coherently coupled weak resonances, Sci. Bull. **65**, 373 (2020).

[27] N. Jiménez, V. Romero-García, V. Pagneux, and J.-P. Groby, Rainbow-trapping absorbers: Broadband, perfect and asymmetric sound absorption by subwavelength panels for transmission problems, Sci. Rep. **7**, 13595 (2017).

[28] D. Li, S. Huang, Y. Cheng, and Y. Li, Compact asymmetric sound absorber at the exceptional point, Sci. China Phys. Mech. Astron. **64**, 244303 (2021).

[29] Y. X. Gao, Y. Cheng, B. Liang, Y. Li, J. Yang, and J. C. Cheng, Acoustic skin meta-muffler, Sci. China Phys. Mech. Astron. **64**, 294311 (2021).

[30] Y. Zhu, A. Merkel, K. Donda, S. Fan, L. Cao, and B. Assouar, Nonlocal acoustic metasurface for ultrabroadband sound absorption, Phys. Rev. B **103**, 064102 (2021).

[31] Y. Xie, C. Shen, W. Wang, J. Li, D. Suo, B. I. Popa, Y. Jing, and S. A. Cummer, Acoustic holographic rendering with two-dimensional metamaterial-based passive phased array, Sci. Rep. **6**, 35437 (2016).

[32] Y. Zhu, J. Hu, X. Fan, J. Yang, B. Liang, X. Zhu, and J. Cheng, Fine manipulation of sound via lossy metamaterials with independent and arbitrary reflection amplitude and phase, Nat. Commun. **9**, 1632 (2018).

[33] R. Fleury, A. B. Khanikaev, and A. Alù, Floquet topological insulators for sound, Nat. Commun. **7**, 11744 (2016).

[34] Z. Zhang, Q. Wei, Y. Cheng, T. Zhang, D. Wu, and X. Liu, Topological Creation of Acoustic Pseudospin Multipoles in a Flow-Free Symmetry-Broken Metamaterial Lattice, Phys. Rev. Lett. **118**, 084303 (2017).

[35] Y. Ding, Y. Peng, Y. Zhu, X. Fan, J. Yang, B. Liang, X. Zhu, X. Wan, and J. Cheng, Experimental Demonstration of Acoustic Chern Insulators, Phys. Rev. Lett. **122**, 014302 (2019).

[36] R. Dong, M. Sun, F. Mo, D. Mao, X. Wang, and Y. Li, Recent advances in acoustic ventilation barriers, J. Phys. D: Appl. Phys. **54**, 403002 (2021).

[37] T. Lee, T. Nomura, E. M. Dede, and H. Iizuka, Ultrasparse Acoustic Absorbers Enabling Fluid Flow and Visible-Light Controls, Phys. Rev. Appl. **11**, 024022 (2019).

[38] H. Zhang, Y. Zhu, B. Liang, J. Yang, J. Yang, and J. C. Cheng, Omnidirectional ventilated acoustic barrier, Appl. Phys. Lett. **111**, 203502 (2017).

[39] R. Ghaffarivardavagh, J. Nikolajczyk, S. Anderson, and X. Zhang, Ultra-open acoustic metamaterial silencer based on Fano-like interference, Phys. Rev. B **99**, 024302 (2019).

[40] X. Xiang, X. Wu, X. Li, P. Wu, H. He, Q. Mu, S. Wang, Y. Huang, and W. Wen, Ultra-open ventilated metamaterial absorbers for sound-silencing applications in environment with free air flows, Extreme Mech. Lett. **39**, 100786 (2020).

[41] R. Dong, D. Mao, X. Wang, and Y. Li, Ultrabroadband Acoustic Ventilation Barriers via Hybrid-Functional Metasurfaces, Phys. Rev. Appl. **15**, 024044 (2021).

[42] L. Shen, Y. Zhu, F. Mao, S. Gao, Z. Su, Z. Luo, H. Zhang, and B. Assouar, Broadband Low-Frequency Acoustic Metamuffler, Phys. Rev. Appl. **16**, 064057 (2021).
[43] M. Sun, X. Fang, D. Mao, X. Wang, and Y. Li, Broadband Acoustic Ventilation Barriers, Phys. Rev. Appl. **13**, 044028 (2020).
[44] R. Dong, D. Mao, Y. Zhu, F. Mo, X. Wang, and Y. Li, A ventilating acoustic barrier for attenuating broadband diffuse sound, Appl. Phys. Lett. **119**, 263505 (2021).
[45] C. Liu, H. Wang, B. Liang, J. C. Cheng, and Y. Lai, Low-frequency and broadband Muffler via cascaded labyrinthine metasurfaces, Appl. Phys. Lett. **120**, 231702 (2022).
[46] C. Liu, J. Shi, W. Zhao, X. Zhou, C. Ma, R. Peng, M. Wang, Z. Hang, X. Liu, J. Christensen, N. X. Fang, and Y. Lai, Three-Dimensional Soundproof Acoustic Metacage, Phys. Rev. Lett. **127**, 084301 (2021).
[47] L. Quan and A. Alù, Hyperbolic Sound Propagation over Nonlocal Acoustic Metasurfaces, Phys. Rev. Lett. **123**, 244303 (2019).
[48] ASTM E2611-09, standard test method for measurement of normal incidence sound transmission of acoustical materials based on the transfer matrix method (American Society for Testing and Materials, 2009).